Acta Cryst F STRUCTURAL BIOLOGY COMMUNICATIONS
ISSN 2053-230X

Crystal structures of the amino-terminal domain of LpoA from *Escherichia coli* and *Haemophilus influenzae*

Aaron Kelley,[a] J. Vijayalakshmi[b] and Mark A. Saper[a,b]*

[a]Department of Biological Chemistry, University of Michigan, 1150 West Medical Center Drive, Ann Arbor, MI 48109-5606, USA, and [b]Program in Biophysics, University of Michigan, 930 North University Avenue, Ann Arbor, MI 48109-1055, USA. *Correspondence e-mail: saper@umich.edu

Received 17 January 2019
Accepted 24 March 2019

Edited by S. Sheriff, Bristol-Myers Squibb, USA

Keywords: outer membrane lipoprotein; peptidoglycans; TPR domain; conformational differences; LpoA; N-terminal domains.

PDB references: amino-terminal domain of *H. influenzae* LpoA, 6dcj; amino-terminal domain of *E. coli* LpoA, 6dr3

Supporting information: this article has supporting information at journals.iucr.org/f

The bacterial periplasmic protein LpoA is an outer membrane lipoprotein and an activator for the cross-linking activity of PBP1A, a bifunctional peptidoglycan synthase. Previous structures of the amino-terminal (N) domain of LpoA showed it to consist entirely of helices and loops, with at least four tetratricopeptide-like repeats. Although the previously determined orthorhombic crystal structure of the N domain of *Haemophilus influenzae* LpoA showed a typical curved structure with a concave groove, an NMR structure of the same domain from *Escherichia coli* was relatively flat. Here, a crystal structure of the N domain of *E. coli* LpoA was determined to a resolution of 2.1 Å and was found to be more similar to the *H. influenzae* crystal structure than to the *E. coli* NMR structure. To provide a quantitative description for these comparisons, the various structures were superimposed pairwise by fitting the first half of each structure to its pairwise partner and then calculating the rotation axis that would optimally superimpose the second half. Differences in both the magnitude of the rotation and the direction of the rotation axis were observed between different pairs of structures. A 1.35 Å resolution structure of a monoclinic crystal form of the N domain of *H. influenzae* LpoA was also determined. In this structure, the subdomains rotate 10° relative to those in the original orthorhombic *H. influenzae* crystal structure to further narrow the groove between the subdomains. To accommodate this, a bound chloride ion (in place of sulfate) allowed the closer approach of a helix that forms one side of the groove.

1. Introduction

Bacterial cell walls are primarily comprised of peptidoglycan (PG), a polymer of disaccharides cross-linked through peptide substituents. PG provides protection against internal osmotic pressure (turgor), functions in cell division and defines cell shape. Besides the recently characterized PG polymerase RodA encoded by most bacteria (Meeske *et al.*, 2016), Gram-negative bacteria also require a bifunctional enzyme, specifically either PBP1A or PBP1B, which can polymerize and cross-link PG and may play a role in PG repair. LpoA is an outer membrane lipoprotein that is essential for activating the cross-linking (transpeptidase) activity of PBP1A (Typas *et al.*, 2010; Paradis-Bleau *et al.*, 2010). LpoA is composed of two domains: a primarily helical amino-terminal (N) domain and a carboxyl-terminal domain involved in interactions with PBP1A. Analyses of multiple crystal structures of full-length LpoA from *Haemophilus influenzae* (*Hi*LpoA), together with small-angle X-ray scattering results, suggested that LpoA is a flexible molecule that is capable of extending through gaps or holes in PG in order to interact with the inner-membrane-bound PBP1A (Sathiyamoorthy *et al.*, 2017). Although the

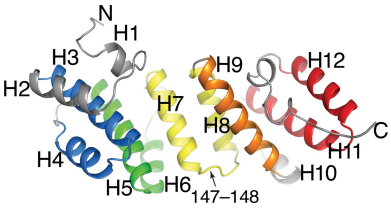

Table 1
Expression plasmid construction.

	*Ec*Tet (31–252)	*Hi*Mon (33–253)
Source organism	*E. coli* MG1655	*H. influenzae* Rd
DNA source	pCB40 plasmid DNA (Paradis-Bleau *et al.*, 2010)	*H. influenzae* Rd genomic DNA
Cloning method	Isothermal (NEBuilder HiFi, NEB)	Restriction enzymes
Forward primer	agaacctgtacttccAATCCACTCCCGATCAGTCCACTG†	CATGCCATGGCGAATTTCACGCAAACCTTACAA‡
Reverse primer	cgttatccacttccaatattttaTTTAAACGCTTTTACGTTA ACCAAC†	GCCGACGTCGACTTGTTGGAAATTAAGCAATGTAAG§
Forward primer to amplify plasmid	taaAATATTGGAAGTGGATAACGGATC	
Reverse primer to amplify plasmid	GGATTGGAAGTACAGGTTCTCG	
Cloning vector	pMCSG7 (Stols *et al.*, 2002)	pETBlue-2 (Novagen)
Expression vector	pMCSG7	pETBlue-2
Expression host	*E. coli* Origami 2(DE3) (Novagen)	*E. coli* Tuner(DE3)/pLacI (Novagen)
Complete amino-acid sequence of the construct produced	mhhhhhhssgvdlgtenlyfqSTPDQSTAYMQGTAQADSAFY LQQMQQSSDDTRINWQLLAIRALVKEGKTGQAVELFNQLP QELNDAQRREKTLLAVEIKLAQKDFAGAQNLLAKITPADL EQNQQARYWQAKIDASQGRPSIDLLRALIAQEPLLGAKEK QQNIDATWQALSSMTQEQANTLVINADENILQGWLDLQRV WFDNRNDPDMMKAGIADWQKRYPNNPGAKMLPTQLVNVKA FK¶	MANFTQTLQKDANASSEFYINKLGQTQELEDQQTYKLLAARV LIRENKVEQSAALLRELGELNDAQKLDRALIEARISAAKN ANEVAQNQLRALDLNKLSPSQKSRYYETLAIVAENRKDMI EAVKARIEMDKNLTDVQRHQDNIDKTWALLRSANTGVINN ASDEGNAALGGWLTLIKAYNDYIRQPVQLSQALQSWKNAY PNHAAATLFPKELLTLLNFQQVEHHHHHH††

† The primer 5′ extensions shown in lower case base-pair with sequences on the linearized plasmid for the isothermal cloning procedure. ‡ The NcoI site for cloning is underlined. § The SalI site for cloning is underlined. ¶ Lower case indicates the sequence in *Ec*Tet (31–252) that was removed after TEV proteolysis. †† The underlined N-terminal MA and C-terminal His_6-tag residues were added to the native sequence during cloning.

interdomain linker is responsible for much of the flexibility of the molecule, twists and bends of up to 5° have been observed within the N domain and are likely to affect the overall length of the molecule.

The structures of the N domain from both *E. coli* LpoA (*Ec*LpoA) and *Hi*LpoA contain repeats of the helical tetratricopeptide-like (TPR-like) motif, which is a helix–turn–helix motif that is often involved in protein–protein interactions. Consecutive TPR-like motifs typically induce a superhelical twist to form a concave groove that is ideal for binding peptide segments of other proteins (Grove *et al.*, 2008). For example, a conformational change of the TPR-containing protein MamA is associated with binding of its putative ligand, suggesting possible mechanisms for TPR-regulated functionality (Zeytuni *et al.*, 2011).

The structure of the N domain of *E. coli* LpoA was first determined using NMR (*Ec*NMR) and, although composed of TPR-like helix–turn–helix motifs, was observed to be relatively flat without a significant superhelical twist (Jean *et al.*, 2014). When the orthorhombic crystal structure of the N domain of *H. influenzae* LpoA (*Hi*Ort) was reported (Sathiyamoorthy *et al.*, 2017), its subdomains 1 and 2 were noted to each be very similar to the corresponding subdomains in *Ec*NMR. However, when the two intact N-domain structures were superimposed, based solely on least-squares fitting of their subdomains 1 (specifically residues 33–148), their subdomains 2 were related by a 45° rotation (see Fig. 2 in Sathiyamoorthy *et al.*, 2017).

To better understand the range of conformations accessible to the LpoA N domain, we set out to determine its structure in additional crystal environments. We determined the tetragonal crystal structure of the N domain of *Ec*LpoA (*Ec*Tet) and found it to be closer in structure to *Hi*Ort than to *Ec*NMR. We also determined a 1.35 Å resolution structure of the N domain of *Hi*LpoA in a monoclinic space group; inspection of this structure showed it to have a more concave cleft than the previously reported orthorhombic form (PDB entry 4p29; Sathiyamoorthy *et al.*, 2017).

2. Materials and methods

2.1. Macromolecule production

To express the *Ec*LpoA N domain, the gene corresponding to residues 31–252 of *Ec*LpoA was amplified using PCR from genomic DNA (*E. coli* strain MG1655) and cloned into pMCSG7 (Stols *et al.*, 2002). The primers used to amplify the domain from *Ec*LpoA and to linearize the pMCSG7 plasmid are shown in Table 1. The resulting construct contained an N-terminal His_6 tag and TEV protease cleavage site (detailed in Table 1). The construct was confirmed by carrying out Sanger sequencing in both the forward and reverse directions.

The pMCSG7-*Ec*LpoA-N plasmid was transformed into *E. coli* Origami 2(DE3) cells (Novagen). The cells were grown in two 2.8 l flasks, each containing 450 ml Terrific Broth. After inoculation and initial growth, the flasks were transferred to an incubator at 22°C and IPTG was added to 0.45 m*M* for induction. The cells were harvested 16 h after induction by centrifugation at 5900*g*, after which they were resuspended with DNase and protease-inhibitor tablets and frozen at −80°C. The cells were lysed via three passes through an Emulsiflex-C3 homogenizer at 4°C. The clarified lysate was applied onto a 5 ml column packed with HisPur Cobalt Resin (Thermo Fisher), washed and then eluted with 180 m*M* imidazole. The protein was treated with TEV protease overnight at 4°C and then passed through a HisPur Ni–NTA Resin column (Thermo Fisher) to remove cleaved His_6 tag and TEV protease. Concentrated protein (25 mg ml^{-1}) was frozen in aliquots containing 10% glycerol. Before crystallization trials, the aliquots were passed through a gel-filtration column (Superdex HR 75 10/300) to remove glycerol. The predicted sequence of the mature *Ec*LpoA N-domain protein was serine

Table 2
Crystallization.

	*Ec*Tet (31–252)	*Hi*Mon (33–253)
Method	Sitting-drop vapor diffusion	Hanging-drop vapor diffusion
Plate type	24-well sitting drop	Linbro (Hampton Research)
Temperature (K)	295	295
Protein concentration (mg ml^{-1})	19	10
Buffer composition of protein solution	150 m*M* NaCl, 25 m*M* Tris–HCl pH 7.5	0.1% β-mercaptoethanol, 1 m*M* EDTA, 0.1 m*M* benzamidine, 20 m*M* Tris–HCl pH 8.0
Composition of reservoir solution	0.03 *M* magnesium chloride hexahydrate, 0.03 *M* calcium chloride dihydrate, 5% glycerol, 10% PEG 20 000, 17% PEG monomethyl ether 550, 0.1 *M* Buffer System 1 pH 6.5†	20% polyethylene glycol (PEG) 10 000, 0.1 *M* HEPES pH 7.5
Volume and ratio of drop	2 µl, 1:1	
Volume of reservoir	1 ml	

† Buffer System 1, 1.0 *M* stock solution: 30 ml 1 *M* 2-(*N*-morpholino)ethanesulfonic acid (MES) pH 3.1 was titrated with 24.1 ml 1 *M* imidazole pH 10.2 to a final pH of 6.5.

followed by residues 31–252 of *Ec*LpoA (formula weight 25 154).

The cloning, expression and purification of residues 33–253 of the *Hi*LpoA N domain were identical to the procedures described previously (Sathiyamoorthy *et al.*, 2017). The gene fragment with NcoI and SalI restriction sites corresponding to residues 33–253 of *Hi*LpoA was amplified using PCR from genomic DNA isolated from the *H. influenzae* Rd strain (ATCC catalog No. 9008). After digestion, the purified fragment was ligated into the pETBlue-2 (Novagen) plasmid. The plasmid encoding the N-terminal residues MA and the C-terminal His_6 tag was transformed into *E. coli* Tuner(DE3)/pLacI (Novagen) cells for expression. The formula weight of the purified protein was predicted to be 26 224. Details of the construct are shown in Table 1.

2.2. Crystallization

Initial crystals of the N domain of *Ec*LpoA grew from condition A1 of the Morpheus screen (Molecular Dimensions). The N domain of *Hi*LpoA was previously reported to form orthorhombic crystals (Sathiyamoorthy *et al.*, 2017). In the current work, we grew monoclinic crystals of the N domain of *Hi*LpoA from different conditions. Crystals were harvested into precipitant containing 10% glycerol and were immediately cooled in liquid nitrogen. Crystallization information is given in Table 2.

2.3. Data collection and processing

Diffraction data were collected from the tetragonal crystals of the N domain of *Ec*LpoA (*Ec*Tet) on the LS-CAT beamline 21-ID-D at the Advanced Photon Source (APS), Argonne National Laboratory and were processed with *HKL*-2000 (Otwinowski & Minor, 1997). Diffraction data for the monoclinic crystals of the N domain of *Hi*LpoA (*Hi*Mon) were collected on the DND-CAT beamline 5-ID-B at APS and were processed with *d*TREK* (Pflugrath, 1999). Details of data collection and processing are presented in Table 3.

2.4. Structure solution and refinement

Initial attempts to solve the structure of *Ec*Tet by molecular replacement in *Phaser* (McCoy *et al.*, 2007; Adams *et al.*, 2010) with search models containing each subdomain of *Ec*NMR (PDB entry 2mhk; Jean *et al.*, 2014) were unsuccessful. The two subdomains of *Hi*Ort (29% sequence identity to *Ec*Tet), after pruning side chains that were not common with *Ec*Tet in *Sculptor* (Bunkóczi & Read, 2011), were used as search models. Molecular-replacement calculations in *Phaser* resulted in a log-likelihood gain (LLG) of 312 and a translation-function *Z*-score (TFZ) of 17.1, and confirmed that the space group for these data was $P4_32_12$. The structure was manually built with *Coot* (Emsley *et al.*, 2010) and refined in *PHENIX* (v.1.12; Adams *et al.*, 2010) with data to 2.1 Å resolution (99% complete) and three TLS domains to a final R_{work} and R_{free} of 0.177 and 0.213, respectively. Waters were added and validated in *Coot*. Simulated-annealing OMIT maps were consulted to minimize the bias from the starting model (Supplementary Fig. S1). Details of the refinement and model validation are summarized in Table 4. The coordinates and structure factors were deposited in the PDB as entry 6dr3. Residue numbering corresponds to that of GenBank sequence NP_417616.1 and not to the sequence numbering for *Ec*NMR (PDB entry 2mhk).

In solving the *Hi*Mon structure, molecular-replacement calculations with *Phaser* using the intact structure of *Hi*Ort (PDB entry 4p29) as a search model (Sathiyamoorthy *et al.*, 2017) were unsuccessful. Breaking the search model into two subdomains as above successfully placed two copies of each of the two subdomains in the asymmetric unit, consistent with two monomers. The LLG and TFZ values were 2681 and 33.3, respectively, for the molecular-replacement solution. As above, the *Hi*Mon structure was modified in *Coot* and refined with *PHENIX* with data to 1.35 Å resolution (90% complete) and anisotropic *B* factors to a final R_{work} and R_{free} of 0.155 and 0.190, respectively. TLS refinement was not performed as it was redundant with the anisotropic *B* factors. Hydrogens were included in their riding positions. Details of the refinement and model validation are summarized in Table 4 and an OMIT map is shown in Supplementary Fig. S2. Coordinates and structure factors were deposited in the PDB as entry 6dcj.

2.5. Structure comparisons

All structural superimpositions were performed by least-squares fitting using the *super* routine of *PyMOL* (v.2.2;

Table 3
Data collection and processing.

Values in parentheses are for the outer shell.

	*Ec*Tet (31–252)	*Hi*Mon (33–253)
Diffraction source	Beamline 21-ID-D, LS-CAT, APS	Beamline 5-ID-B, DND-CAT, APS
Wavelength (Å)	0.9772	0.9793
Temperature (K)	140	140
Detector	Dectris EIGER X 9M	MAR MX225 CCD
Crystal-to-detector distance (mm)	250	150.8
Rotation range per image (°)	0.5	0.8
Total rotation range (°)	200	180
Exposure time per image (s)	0.25	6
Space group	$P4_32_12$	$P2_1$
a, b, c (Å)	70.001, 70.001, 97.802	68.988, 36.927, 95.359
α, β, γ (°)	90, 90, 90	90, 108.08, 90
Mosaicity (°)	0.30–0.49	0.55–1.03
Resolution range (Å)	22.7–2.10 (2.18–2.10)	34.50–1.35 (1.40–1.35)
Total No. of reflections	160658 (8220)	301389 (12818)
No. of unique reflections	14746 (1368)	91428 (6067)
Completeness (%)	99.23 (94.08)	90.3 (59.9)
Redundancy	10.9 (5.7)	3.28 (2.13)
$\langle I/\sigma(I)\rangle$	17.14 (2.13)	13.1 (2.9)
R_{meas}	0.116 (0.829)	0.055 (0.314)†
$CC_{1/2}$	0.998 (0.715)	‡
Overall B factor from Wilson plot (Å^2)	27	16

† For the N domain of *Hi*LpoA , the redundancy-independent merging R factor R_{meas} was calculated by multiplying the R_{merge} value of 0.046 by $[N/(N-1)]^{1/2}$, where N is the data redundancy. ‡ Not available.

Table 4
Structure solution and refinement.

Values in parentheses are for the outer shell.

	*Ec*Tet (31–252)	*Hi*Mon (33–253)
PDB entry	6dr3	6dcj
Resolution range (Å)	22.7–2.10 (2.18–2.10)	34.44–1.35 (1.40–1.35)
Completeness (%)	99.23 (94.08)	90.52 (60.70)
σ Cutoff	None	None
No. of reflections, working set	13194 (1230)	91406 (6065)
No. of reflections, test set	1465 (137)	7328 (490)
Final R_{cryst}	0.177 (0.249)	0.155 (0.228)
Final R_{free}	0.213 (0.280)	0.190 (0.279)
No. of non-H atoms		
Protein	1776	3652
Ion	0	2
Water	151	714
Total	1927	4368
R.m.s. deviations		
Bonds (Å)	0.002	0.007
Angles (°)	0.44	1.17
Average B factors (Å^2)		
Overall	38	25†
Protein	38	22
Ion	n.a.	21
Water	40	35
Ramachandran plot		
Most favored (%)	97.29	99.54
Allowed (%)	2.71	0.46
Rotamer outliers (%)	0.53	0.51
MolProbity score/clashscore	1.01/1.41	1.03/2.46

† The *Hi*Mon structure was refined with anisotropic B factors. Isotropic equivalent values are shown in this table.

Schrödinger). This routine in *PyMOL* iteratively rejects paired residues if the interatomic distance exceeds two times the overall r.m.s. deviation. Object transformation matrices from *super* were converted into an equivalent angular rotation about a screw axis (*GEM*; E. Fauman, unpublished work), which was displayed as a cylindrical arrow using a compiled graphics object in *PyMOL*. To ascertain the difference in curvature (the relative difference in subdomain 2 rotation) between two LpoA N-domain structures, subdomains 1 of the structures were first superimposed. Subdomains 2 were then superimposed and the matrix from this latter transformation was converted into an equivalent rotation as above. All figures were prepared in *PyMOL*.

3. Results

3.1. Comparison of *Ec*Tet and *Ec*NMR (PDB entry 2mhk)

As described in Section 2, the protein that was crystallized to form *Ec*Tet was designed to include Ser30 followed by residues 31–252 of *Ec*LpoA. Two subdomains consisting of 13 helices and the loops between them were observed in *Ec*Tet, with subdomain 1 consisting of helices H1–H7 and spanning residues 30–147 and subdomain 2 consisting of helices H8–H13 and spanning residues 148–252 (Fig. 1). Residues 242–247 form one turn of an α-helix, while two turns were observed in both *Ec*NMR and *Hi*Ort. Only weak density was observed corresponding to residues 247–252, indicating that these residues were likely to be partially disordered.

Subdomains 1 and 2 of *Ec*Tet were individually superimposed on the respective subdomains of *Ec*NMR, and analysis of this superposition confirmed similar local folds (subdomain 1, r.m.s.d. on C^α atoms of 2.0 Å; subdomain 2, r.m.s.d. on C^α atoms of 1.5 Å; see Table 5). However, superimposing the full-length N domains showed quite a large difference in backbone structure (r.m.s.d. of 3.5 Å), with this difference explained by different rotations between the two

subdomains in the two structures. The difference in domain curvature (calculated as described in Section 2) showed that *Ec*NMR subdomain 2 required a 33° rotation around the axis displayed in Fig. 2 in order to optimally superimpose it onto *Ec*Tet. That is, in contrast to *Ec*NMR, *Ec*Tet was observed to exhibit more of a superhelical twist and a more pronounced concave groove between the two subdomains.

3.2. Comparison of the overall conformations of *Ec*Tet and *Hi*Ort

After aligning subdomain 1 of the *Ec*Tet crystal structure onto that of *Hi*Ort, subdomain 2 of *Ec*Tet must be rotated by 17.4° around the axis shown in Fig. 3 to superimpose it on subdomain 2 of *Hi*Ort. That is, the *Ec*Tet concave curvature, while more pronounced than that for *Ec*NMR, was observed

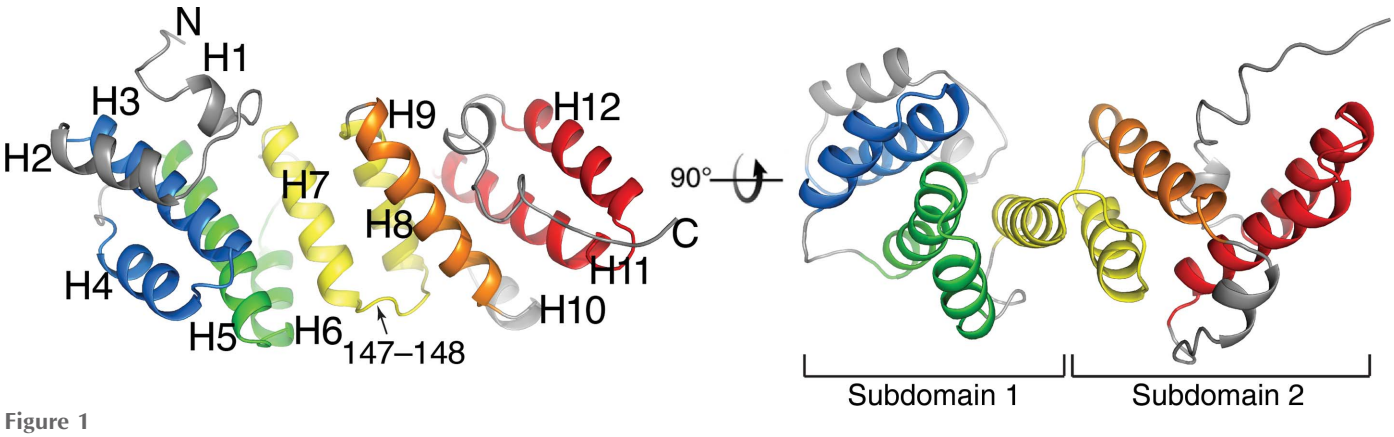

Figure 1
Cartoon representation of the *Ec*Tet domain, highlighting the TPR-like motifs in different colors. Left, top view looking into the groove located above helix H7. Right, side view showing the concave shape of the domain and the locations of the subdomains.

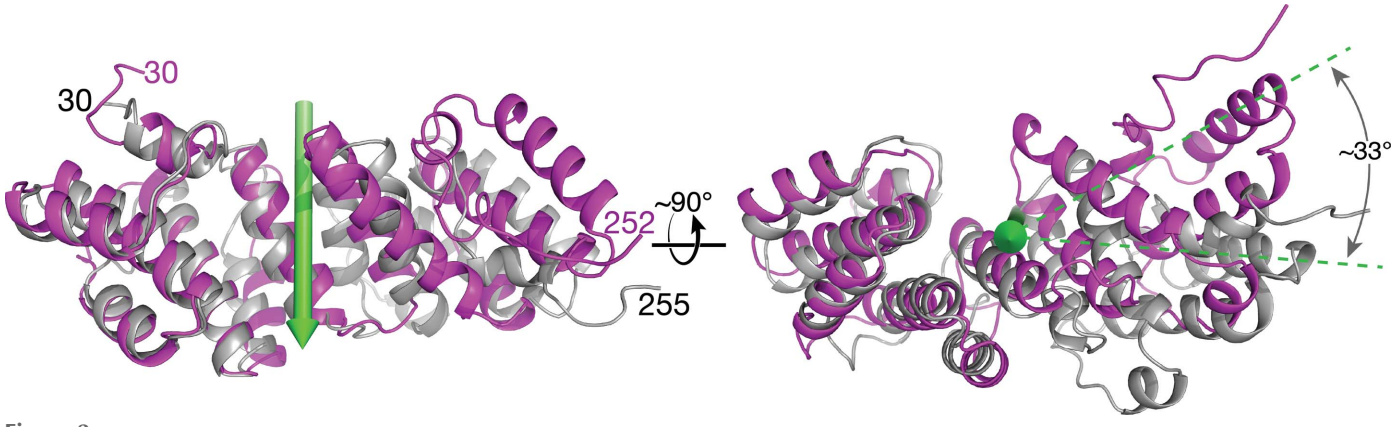

Figure 2
Superimposition of the *Ec*NMR structure (gray) and the *Ec*Tet crystal structure (magenta) accomplished by fitting their subdomains 1. The green cylindrical arrow indicates the 33° rotation axis relating the subdomains 2 of the two superimposed structures. Right, side view showing the rotation axis end-on.

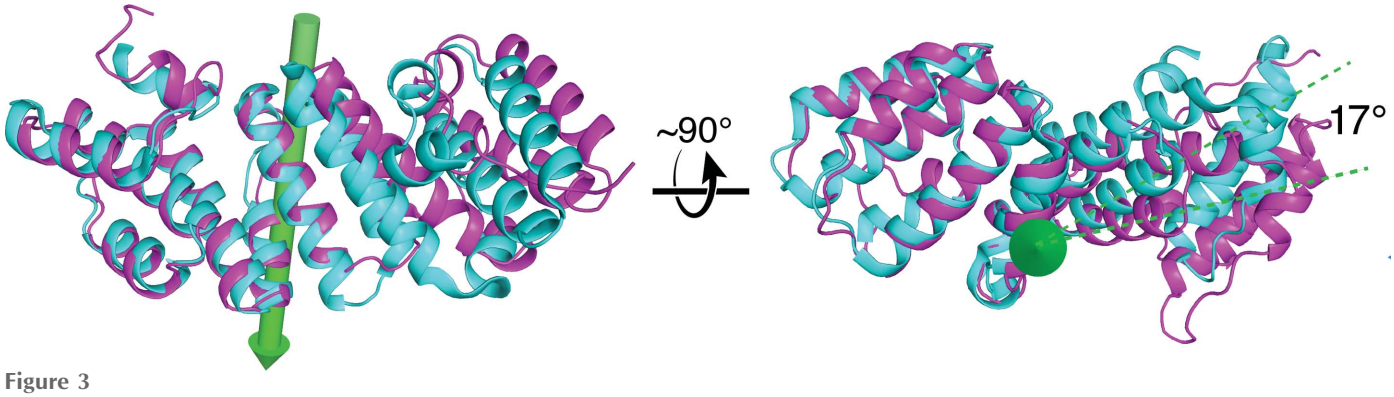

Figure 3
Superimposition of *Hi*Ort (cyan) and *Ec*Tet (magenta) accomplished by fitting their subdomains 1. Right, side view showing the 17° rotation between the respective subdomains 2.

Table 5
Summary of structural comparisons of LpoA N domains.

Aligned structures	R.m.s.d.† (Å)			Rotation‡ (°)	Translation§ (Å)
	Overall	Subdomain 1	Subdomain 2		
*Ec*NMR/*Ec*Tet	3.7 (209/222)	2.0 (112/118)	1.5 (94/105)	33	0.4
*Hi*Ort/*Ec*Tet	2.4 (199/221)	0.9 (82/118)	0.8 (77/104)	17	0.0
*Hi*Mon/*Ec*Tet	3.2 (206/221)	1.0 (99/116)	1.2 (77/104)	27	−1.0
*Hi*Ort/*Hi*Mon	1.0 (207/221)	0.3 (96/116)	0.4 (80/105)	10	−0.5

† Values in parentheses are (number of C^{α} atoms superimposed/total number of C^{α} atoms). ‡ The rotation of subdomain 2 along the inter-subdomain screw axis relative to subdomain 1. § The translation along the inter-subdomain screw axis.

to be less prominent than that of *Hi*Ort. A similar comparison with the high-resolution *Hi*Mon structure (see Section 3.3 below) required a 27° rotation around a similar axis in order for *Ec*Tet subdomain 2 to best superimpose on that of *Hi*Mon (Table 5).

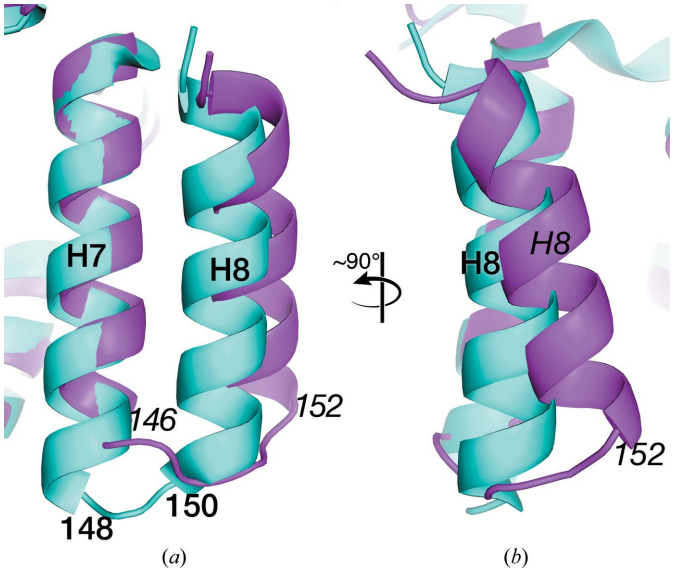

Figure 4
Helices H7 and H8 from both *Hi*Ort (cyan) and *Ec*Tet (magenta) after fitting their subdomains 1. A front view (*a*) and side view (*b*) show H7 and H8 to be mostly parallel in *Hi*Ort, but H8 is rotated by about 25° in *Ec*Tet, requiring a longer loop (residues 146–152) between the two helices.

The differences between the overall conformations of *Ec*Tet and *Hi*Ort coincided with, and may have originated from, differences between the junctions of their two subdomains, specifically the loop between helices H7 and H8. Inspection of *Hi*Ort (cyan) showed its H7 and H8 helical axes to be parallel to each other and the loop between the helices (residues 148-RKD-150) to be relatively short (Fig. 4*a*). Inspection of the *Ec*Tet structure (magenta) showed its H8 helix to make an angle of approximately 25° with H7 and the loop between them (residues 146-SQGRPSI-152) to be longer (Fig. 4*b*). The inspection also showed its H7 helix to be about one turn shorter than H7 in *Hi*Ort. The change in conformation is not explained by the differences in the loop sequence. The difference between the interhelix angles of *Ec*Tet and *Hi*Ort appeared to be consistent with the different rotational relationships between their two subdomains.

3.3. Comparison of *Hi*Mon with *Hi*Ort

As for *Hi*Ort (PDB entry 4p29; Sathiyamoorthy *et al.*, 2017), the *Hi*Mon crystal structure was also found to contain two molecules per asymmetric unit. In *Hi*Mon, molecules *A* and *B* superimposed with an r.m.s.d. of 0.3 Å for 194 C^{α} atoms of a total of 211 residues in each molecule. *Hi*Mon molecules *A* and *B* were calculated to be related by a local 176° rotation axis and a 12.2 Å translation along an axis parallel to, but not coincident with, the crystallographic *b* axis. Moreover, β-turn 189–192 appeared to be better ordered in molecule *A* than in molecule *B*, which is likely to be because of the crystal-packing

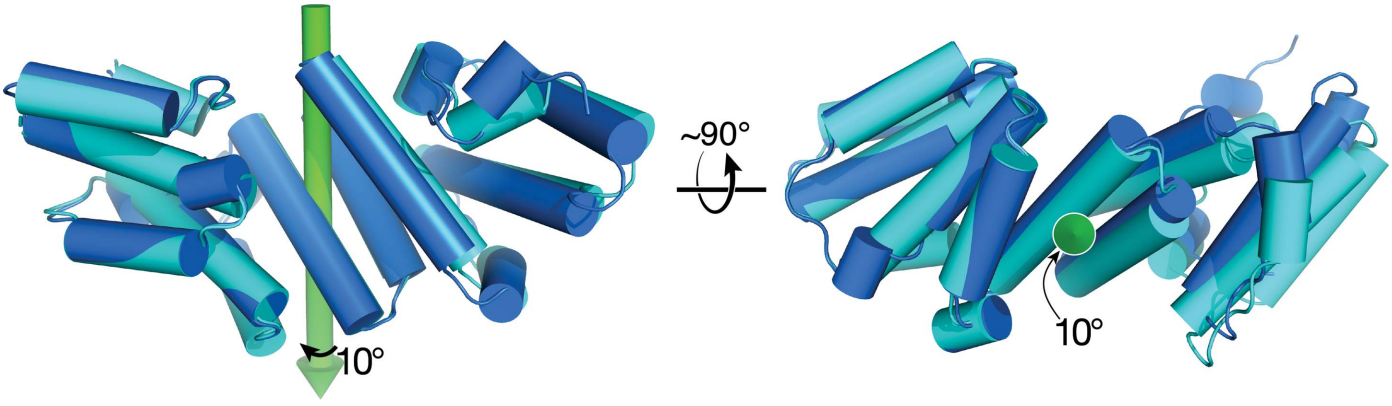

Figure 5
Superimposition of *Hi*Mon (blue) on the previously reported *Hi*Ort structure (cyan) accomplished by fitting their subdomains 1, and showing the 10° rotation axis necessary to then optimally superimpose their subdomains 2.

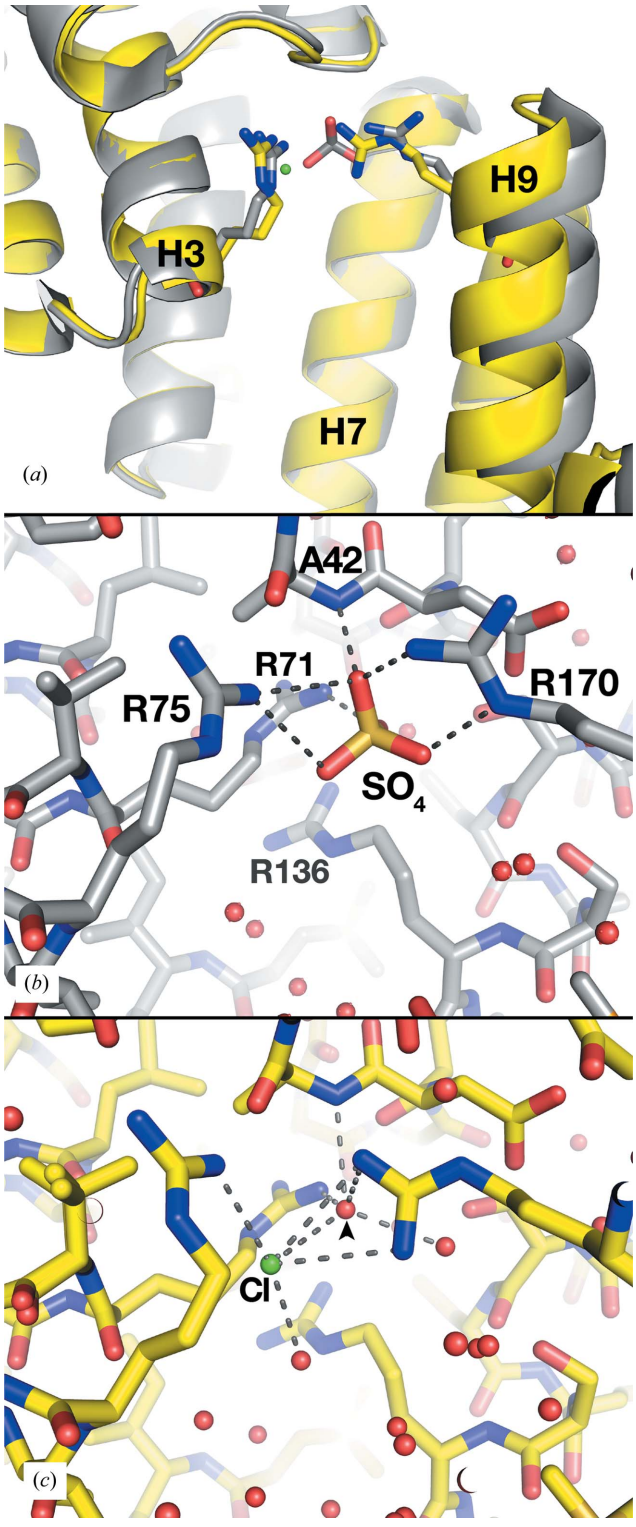

Figure 6
Superimposition of *Hi*Mon (yellow) on *Hi*Ort (gray) suggesting that their binding of different anions can accommodate the different widths of their grooves. (*a*) Both structures are shown with the location of the sulfate bound in the groove of *Hi*Ort and the chloride (green sphere) in *Hi*Mon. (*b*) Close-up view of sulfate (SO_4) ligated to arginine residues 75, 170 and 71 of *Hi*Ort. (*c*) Close-up view of chloride (Cl) bound in the *Hi*Mon structure. Chloride was modeled as the bound anion in *Hi*Mon because the density was significantly larger than a water molecule, chloride was the only anion present in crystallization solutions and the distances to neighboring atoms were 3.2–3.4 Å.

environment. No interpretable electron density corresponding to residue 216 of either molecule was observed, and hence this residue was omitted from the deposited PDB coordinates.

Since the *A* and *B* molecules were essentially identical in both *Hi*Ort and *Hi*Mon, the respective *B* chains were arbitrarily chosen for comparison here. When subdomains 1 (116 residues, 33–148) from each crystal structure were compared, 96 C^{α} atoms were superimposed with an r.m.s.d. of 0.3 Å. Similarly, for subdomain 2 (149–248, 105 residues) 80 C^{α} atoms were superimposed with an r.m.s.d. of 0.4 Å. Comparing the relative curvatures of the two structures showed that the *Hi*Ort subdomain 2 must be rotated by 10° (with an 0.5 Å translation) about an axis passing approximately through the center of the structure to become well superimposed on subdomain 2 of *Hi*Mon (Fig. 5). This rotation coincided with an increase in the curvature of the domain and a narrowing of the concave cleft.

Previously, we described a positively charged pocket that was underneath helix H3 of *Hi*Ort but was accessible from the concave cleft (Sathiyamoorthy *et al.*, 2017). In that structure we identified a sulfate ion (SO_4) ligated by three arginine side chains (Arg71, Arg75 and Arg170) and a main-chain amide (Ala42) (Fig. 6*b*). In the *Hi*Mon crystals, which were grown in the absence of sulfate, a chloride ion (Cl in Fig. 6*c*) bound instead of sulfate, but was about 2.5 Å closer to Arg75, which assumed a different rotamer. A water molecule (black arrow in Fig. 6*c*) occupied the position of the former sulfate. Also, Arg170 took on a different conformation, which allowed a closer approach to the chloride. This movement of Arg170 coincided with the movement of helix H9 of subdomain 2 closer to H3 of subdomain 1 by 1–2 Å (Fig. 6*a*), which in turn narrowed the concave cleft formed by helices H3 and H9 above helix H7. These observations suggested that the binding of a natural ligand in the cleft of the N domain could affect the overall curvature of the domain.

4. Discussion

The comparison of *Ec*NMR and *Hi*Ort was previously discussed by Sathiyamoorthy *et al.* (2017). Superimposing subdomains 1 or subdomains 2 of each molecule individually showed each of them to have similar C^{α} structures in the two molecules (r.m.s.d. values of 1.6 and 1.7 Å, respectively). However, superimposing the intact molecules based on fitting their subdomains 1 required a substantial additional rotation (45°) of subdomain 2 of one molecule to superimpose it optimally on subdomain 2 of the other molecule. In other words, the relationship between subdomains 1 and 2 in *Ec*NMR was observed to be quite different from this relationship in *Hi*Ort, which is reflective of *Ec*NMR being relatively flat and lacking the superhelical twist observed in *Hi*Ort.

To help judge whether the flat conformation of the N domain of *Ec*LpoA in *Ec*NMR was a necessary consequence of its amino-acid sequence or was rather, at least in part, a consequence of the solution conditions used, we also analyzed the *Ec*Tet crystal structure. The *Ec*Tet crystal structure showed more of a curved than a flat conformation, indicating that the

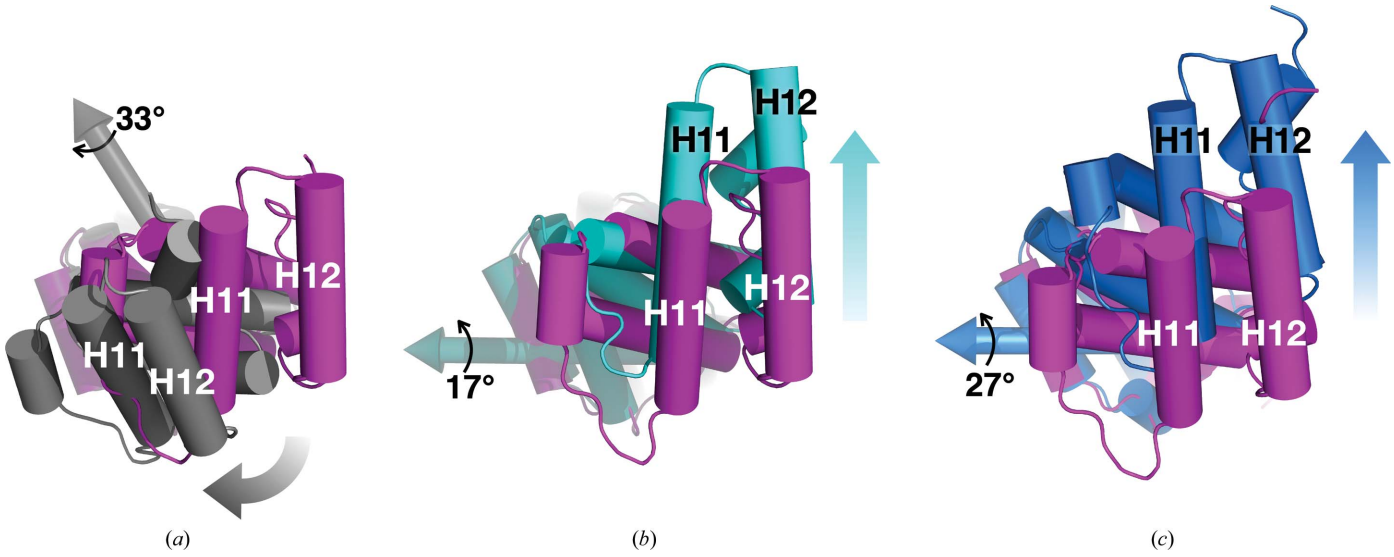

Figure 7
End-on views of structures superimposed on *Ec*Tet (magenta). Also displayed are the rotation axes relating subdomains 2 between *Ec*Tet and the (*a*) *Ec*NMR (gray), (*b*) *Hi*Ort (cyan) and (*c*) *Hi*Mon (blue) structures. The orientations of these axes in the *Hi*Ort and *Hi*Mon crystal structures were found to be similar to each other but significantly different from that in *Ec*NMR.

flat conformation of the *Ec*LpoA N domain observed in the *Ec*NMR solution structure was not mandated by its sequence. Based on the calculated rotation angles to superimpose subdomains 2, the *Ec*Tet crystal structure showed a subdomain 2 orientation intermediate between those of *Hi*Ort and *Ec*NMR. Judging from just these measurements, *Ec*Tet in the crystalline environment appeared to be closer in structure to *Hi*Ort than to *Ec*NMR. However, as shown in Fig. 7, the rotation axis relating subdomains 2 of *Ec*NMR and *Ec*Tet was significantly different from that between *Hi*Ort (or *Hi*Mon) and *Ec*Tet. To further compare the three structures, we measured an interatomic distance between helices H3 and H9 as an indicator of the width of the groove. Despite the large rotation angle relating subdomains 2 of *Ec*Tet and *Ec*NMR, the two structures displayed similar groove widths of 19.5 and 19.7 Å, respectively (not shown; based on the distance between C^{α} of Lys75 and C^{α} of Ala176), while *Hi*Ort displayed a narrower groove with a width of only 15.0 Å (measured between the structurally homologous residues Arg75 and Lys177). The similarity of the groove widths in the *Ec*NMR and *Ec*Tet structures might be explained by the orientation of the rotation axis relating their subdomains 2 (Fig. 7*a*) and its difference from the axis relating subdomains 2 of *Hi*Ort and *Ec*Tet and from the axis relating subdomains 2 of *Hi*Mon and *Ec*Tet (Figs. 7*b* and 7*c*). The effect of the difference can also be observed by the relative positions of H11 and H12 in the two pairs of structures (compare Figs. 7*a* and 7*b*). Analysis of the high-resolution *Hi*Mon structure demonstrated that the domain can assume a more concave structure than previously observed in *Hi*Ort. The groove of *Hi*Mon as defined above was measured to be 1.8 Å narrower than the *Hi*Ort groove.

All of the crystal structures presented here showed a more curved LpoA N domain than was observed in the *Ec*NMR structure. These crystal and NMR structures taken together clearly indicate the N domain to be inherently flexible. Crystal-packing forces may have preferentially selected a more compact structure, but in solution the protein dynamics were less constrained, allowing the molecule to sample other conformations. The intrinsic flexibility of the N domain would be expected to affect the location of the C domain in the intact LpoA structure and its ability to interact with the PBP1A synthase transpeptidase domain in the periplasm, as discussed previously (Sathiyamoorthy *et al.*, 2017).

Acknowledgements

The authors thank Dr Hanseong Kim and Professor Uhn-Soo Cho for help with data collection from the *Ec*Tet crystal and Jerry Brown for his editorial expertise. We thank the outstanding synchrotron support staff at LS-CAT and DND-CAT. This research used resources of the Advanced Photon Source (APS), a US Department of Energy (DOE) Office of Science User Facility operated for the DOE Office of Science by Argonne National Laboratory under Contract No. DE-AC02-06CH11357. LS-CAT Sector 21 was supported by the Michigan Economic Development Corporation and the Michigan Technology Tri-Corridor (grant 085P1000817). The *Hi*Mon data were acquired at the DuPont–Northwestern–Dow Collaborative Access Team (DND-CAT) located at Sector 5 of the APS. DND-CAT is supported by E. I. DuPont de Nemours & Co., The Dow Chemical Company and the State of Illinois.

References

Adams, P. D., Afonine, P. V., Bunkóczi, G., Chen, V. B., Davis, I. W., Echols, N., Headd, J. J., Hung, L.-W., Kapral, G. J., Grosse-Kunstleve, R. W., McCoy, A. J., Moriarty, N. W., Oeffner, R., Read, R. J., Richardson, D. C., Richardson, J. S., Terwilliger, T. C. & Zwart, P. H. (2010). *Acta Cryst.* D**66**, 213–221.
Bunkóczi, G. & Read, R. J. (2011). *Acta Cryst.* D**67**, 303–312.

Emsley, P., Lohkamp, B., Scott, W. G. & Cowtan, K. (2010). *Acta Cryst.* D**66**, 486–501.
Grove, T. Z., Cortajarena, A. L. & Regan, L. (2008). *Curr. Opin. Struct. Biol.* **18**, 507–515.
Jean, N. L., Bougault, C. M., Lodge, A., Derouaux, A., Callens, G., Egan, A. J. F., Ayala, I., Lewis, R. J., Vollmer, W. & Simorre, J.-P. (2014). *Structure*, **22**, 1047–1054.
McCoy, A. J., Grosse-Kunstleve, R. W., Adams, P. D., Winn, M. D., Storoni, L. C. & Read, R. J. (2007). *J. Appl. Cryst.* **40**, 658–674.
Meeske, A. J., Riley, E. P., Robins, W. P., Uehara, T., Mekalanos, J. J., Kahne, D., Walker, S., Kruse, A. C., Bernhardt, T. G. & Rudner, D. Z. (2016). *Nature (London)*, **537**, 634–638.
Otwinowski, Z. & Minor, W. (1997). *Methods Enzymol.* **276**, 307–326.
Paradis-Bleau, C., Markovski, M., Uehara, T., Lupoli, T. J., Walker, S., Kahne, D. E. & Bernhardt, T. G. (2010). *Cell*, **143**, 1110–1120.
Pflugrath, J. W. (1999). *Acta Cryst.* D**55**, 1718–1725.
Sathiyamoorthy, K., Vijayalakshmi, J., Tirupati, B., Fan, L. & Saper, M. A. (2017). *J. Biol. Chem.* **292**, 17626–17642.
Stols, L., Gu, M., Dieckman, L., Raffen, R., Collart, F. R. & Donnelly, M. I. (2002). *Protein Expr. Purif.* **25**, 8–15.
Typas, A., Banzhaf, M., van den Berg van Saparoea, B., Verheul, J., Biboy, J., Nichols, R. J., Zietek, M., Beilharz, K., Kannenberg, K., von Rechenberg, M., Breukink, E., den Blaauwen, T., Gross, C. A. & Vollmer, W. (2010). *Cell*, **143**, 1097–1109.
Zeytuni, N., Ozyamak, E., Ben-Harush, K., Davidov, G., Levin, M., Gat, Y., Moyal, T., Brik, A., Komeili, A. & Zarivach, R. (2011). *Proc. Natl Acad. Sci. USA*, **108**, E480–E487.